Spherical harmonics analysis of Fermi gamma-ray data and the Galactic dark matter halo

Dmitry Malyshev[1], Jo Bovy, and Ilias Cholis

dm137, jb2777, ijc219 @nyu.edu

Center for Cosmology and Particle Physics
4 Washington Place, Meyer Hall of Physics, NYU, New York, NY 10003

ABSTRACT

We argue that the decomposition of gamma-ray maps in spherical harmonics is a sensitive tool to study dark matter (DM) annihilation or decay in the main Galactic halo of the Milky Way. Using the harmonic decomposition in a window excluding the Galactic plane, we show for one year of *Fermi* data that adding a spherical template (such as a line-of-sight DM profile) to an astrophysical background significantly reduces χ^2. In some energy bins the significance of this "DM" fraction is above three sigma.

Assuming a power-law energy spectrum for the backgrounds and the DM component, we find that sources following the stellar mass density or an NFW annihilation profile are preferred to an NFW decay or a bivariate Gaussian profile. We check that the dependence of the DM fraction on the data analysis choices, such as the window size, the pixel size etc. is not significant. We also calculate the contribution from point sources to the variance matrix. Based on the analysis of the angular power spectrum, we indirectly find the average number of photons coming from the multi-photon sources in energy bins above 3 GeV.

[1]On leave of absence from ITEP, Moscow, Russia, B. Cheremushkinskaya 25

1. Motivation

Out of all indirect searches for dark matter (DM), gamma-rays are probably the most "direct" (Zeldovich et al. 1980; Springel et al. 2008a). Charged particles, such as positrons and antiprotons, are deflected in the Galactic magnetic field. The information about their source is lost and only anomalies in the spectrum may signal about the presence of DM. Most of gamma-rays propagate freely inside the Galaxy and, together with the spectrum, they carry information about the morphology of the source. This property may be crucial in separating the DM signal from astrophysical backgrounds (e.g., Siegal-Gaskins & Pavlidou 2009).

From cosmological simulations (e.g., Navarro et al. 1997; Diemand et al. 2008; Kuhlen et al. 2008; Springel et al. 2008b) we expect that Cold dark matter in our Galaxy has formed a nearly spherical halo with density growing towards the Galactic Center (GC). Thus, dark matter annihilation or decay may be a source of gamma-rays with a spherical shape peaked at the GC, in addition to astrophysical and extra-galactic sources.

In this paper, we focus on the contribution from the main spherical halo ignoring DM substructure. In order to maximize the ratio of possible DM signal from the main halo to the astrophysical backgrounds we propose to use the spherical Fourier decomposition of gamma-rays with the z-axis pointing towards the GC. In these coordinates, the Fourier decomposition of the DM line-of-sight density has zero Y_{lm} harmonics for $m \neq 0$, while the DM contribution to Y_{l0} harmonics is maximal. In practice, the astrophysical signal from the Galactic plane and especially from the GC dominates the spherical harmonics for all l and m. In order to maximize the possible DM contribution, we perform the harmonic decomposition in a window above and below the Galactic plane.

In spite of the fact that the isotropic extragalactic background may dominate the signal at high latitude and a small relatively smooth DM contribution may not be visible in coordinate space, the non-isotropic contribution to the Fourier harmonics is proportional to the number of photons, N, while the isotropic distribution, or "noise", contributes as $\sqrt{N}$. Thus even a small Fourier component can be detected for sufficiently many photons.

The main advantages of this approach are:

1. Maximal use of the symmetries of the DM main halo distribution

2. The variance of Fourier harmonics can be calculated explicitly

3. All the information about large scale structure (such as the DM distribution) is encapsulated

in a few small l harmonics. Large l harmonics are dominated by the Poisson noise and do not carry any useful information in this context.

4. All operations on the data are linear. In particular, the χ^2 fit is linear in Fourier space. Also, there is no need for Gaussian smearing of events which leads to information loss additional to the detector Point Spread Function (PSF).

A computational algorithm for fitting in Fourier space is rather straightforward but there are a few things to keep in mind. Firstly, the Y_{lm}'s are not orthogonal in a window on the sphere. The corresponding Fourier modes a_{lm}'s are still independent but correlated such that their variance matrix is not diagonal. In general, this may render the computations unfeasible, unless one uses some special techniques (such as the Gabor transform for the power spectrum; Hansen et al. 2002). We will need only the few Y_{l0} harmonics corresponding to the largest scales. The corresponding variance matrix is relatively small and can be easily computed.

The choice of the astrophysical background model is a more conceptual problem. A thorough solution of this problem can be quite complicated and we will not discuss it here. The main purpose of our work will be to illustrate the method of the Fourier transform in the analysis of gamma-rays. As a toy model for the astrophysical background we will choose the gamma-ray distribution in a low energy bin, since we expect that the DM contribution to the spectrum is insignificant at low energies.

In Section 2 we describe an algorithm of fitting templates in Fourier space. We implement this algorithm using HEALPix (Górski et al. 2005) and perform a Monte Carlo test for the isotropic distribution of photons with a small contribution of DM photons.

In Section 3 we apply this method for every energy bin independently. We compare two cases. In the first case we use two templates: a low energy bin and an isotropic distribution. In the second case we also add a spherical distribution of photons corresponding to DM annihilation in the Navarro, Frenk, and White (NFW) profile (Navarro et al. 1997). We find that the residual for the three-template model is generally compatible with the Poisson noise whereas the residual for the two-template model is significantly larger than the Poisson noise expectation.

In Section 4 we perform a template fit with coefficients scaling as power laws in energy. At first, we consider the two-template model: a low energy bin template and an isotropic background. After that we add various templates with a spherical distribution around the GC. The best fit is obtained for a Galactic stellar halo source, followed, in the order of increasing χ^2, by NFW annihilation, by a Gaussian bivariate sources discussed by Dobler et al. (2010), and by NFW DM

decay. We find that any three-template model fits the data significantly better than the two-template model but the difference in χ^2 among the three-template models is not large enough to draw significant conclusions about the shape of the spherical profile.

In Section 5 we discuss conclusions. There are also two appendices. In Appendix A we study the dependence on various parameters of the model. In Appendix B we discuss the contribution to the Fourier signal from point sources.

2. Method

2.1. Fourier coefficients and their variance

The interpretation of the spherical Fourier decomposition of a DM model is simplest in the coordinate system in which the z-axis points towards the GC (at odds with the standard Galactic coordinates in which the z-axis points towards the Galactic North pole). We will choose the x-axis to point towards the Galactic South pole. We will use the usual spherical coordinates: $\theta \in (0,\, \pi)$ and $\varphi \in (0,\, 2\pi)$, where θ goes from GC to the Galactic anti-center and φ goes around the GC. The Galactic plane corresponds to $\varphi = \pm\frac{\pi}{2}$.

The gamma-ray events in a particular energy bin are represented by a collection of points $\gamma_i = (\theta_i,\, \varphi_i)$. These events can be associated with the observed density function

$$R(\gamma) = \sum_{i=1}^{N} \delta(\gamma - \gamma_i)\,. \tag{1}$$

The spherical Fourier transform of this density function is

$$R_{lm} = \int Y^*_{lm}(\gamma) R(\gamma) d\Omega = \sum_{i=1}^{N} Y^*_{lm}(\gamma_i)\,. \tag{2}$$

In the following we will use a single index k to denote a pair of indices (l, m) parameterizing the spherical harmonics

$$Y_{lm}(\theta,\, \varphi) = \sqrt{\frac{2l+1}{4\pi}\frac{(l-m)!}{(l+m)!}} P_l^m(\cos\theta) e^{im\varphi}\,. \tag{3}$$

The spherical harmonics form an orthonormal basis on the sphere $\int Y^*_k(\gamma) Y_{k'}(\gamma) d\Omega = \delta_{kk'}$, while on a window in the sphere this integral is not diagonal (e.g., Hansen et al. 2002).

Let us estimate the variance (standard deviation) of the Fourier harmonics $R_k \equiv R_{lm}$. Denote by $\delta n = R(\gamma)\delta\Omega$ the number of photons inside a small solid angle $\delta\Omega$. We will assume

a Poisson distribution of photons as a reasonable first approximation. A modification of this derivation due to point sources is calculated in Appendix B.

We decompose the sphere in a collection of small solid angles $\delta\Omega_s$. The average of the random variable R_k is estimated as

$$\langle R_k \rangle = \sum_s Y^*(\gamma_s) \langle R(\gamma_s) \rangle \delta\Omega_s = \sum_s Y^*(\gamma_s) \langle \delta n_s \rangle \,. \tag{4}$$

The variance matrix is

$$V_{kk'} = \langle R_k^* R_{k'} \rangle - \langle R_k^* \rangle \langle R_{k'} \rangle = \sum_s Y_{k'}^*(\gamma_s) Y_k(\gamma_s) \left(\langle \delta n_s^2 \rangle - \langle \delta n_s \rangle^2 \right) \,, \tag{5}$$

where we have used that the numbers of photons at different points are not correlated $\langle \delta n_s \delta n_{s'} \rangle = \langle \delta n_s \rangle \langle \delta n_{s'} \rangle$. For a Poisson distribution $\langle \delta n_s^2 \rangle - \langle \delta n_s \rangle^2 = \langle \delta n_s \rangle$, consequently

$$V_{kk'} = \sum_s Y_{k'}^*(\gamma_s) Y_k(\gamma_s) \langle \delta n_s \rangle \,. \tag{6}$$

If we go back from the finite sum to the integral and take $R(\gamma)$ in Equation (1) as the best estimate of $\langle R(\gamma) \rangle$, then the best estimates of the average $\langle R_k \rangle$ and the variance matrix are

$$R_k = \sum_{i=1}^{N} Y_k^*(\gamma_i) \,, \tag{7}$$

$$V_{kk'} = \sum_{i=1}^{N} Y_{k'}^*(\gamma_i) Y_k(\gamma_i) \,. \tag{8}$$

The harmonic modes carry the information about the photon distribution on angular scales much larger than the detector PSF. At the scale of the PSF both R_k and $V_{kk'}$ should reduce to the Poisson noise. We note that in the derivation we haven't used the reference to the Fourier transform on the whole sphere. These expressions work for a collection of events in a window on the sphere as well.

2.2. Fitting algorithm

In practical calculations we use *healpy*, the python version of HEALPix (Górski et al. 2005) that performs a fast Fourier transform on a pixelation of the sphere.[1] The pixels in HEALPix

[1] `http://code.google.com/p/healpy/` and `http://healpix.jpl.nasa.gov`, respectively.

have areas of equal size $\delta\Omega_{N_{\rm pix}} = \frac{4\pi}{N_{\rm pix}}$ where $N_{\rm pix}$ is the number of pixels. Denote by n_p the number of events in a pixel $p = 1, \ldots, N_{\rm pix}$. In order to get the pixelation of the flux we have to divide n_p by the pixelation of the detector exposure map E_p and by the solid angle $\delta\Omega_{N_{\rm pix}}$

$$F(\gamma_p) = \frac{n_p}{E_p}\frac{1}{\delta\Omega_{N_{\rm pix}}}\,. \tag{9}$$

Alternatively, one can multiply the model fluxes by the exposure to get the counts in the pixels. In some cases this may be a better approach, since we clearly separate the data (the counts) and the models which include the templates and the exposure map. In the case of the *Fermi* data, there are two classes of events: front converted and back converted. The exposure maps for the two classes of events are different. In this paper, we use the front and back converted photons simultaneously and the flux at pixel p is defined as the average between the fluxes derived from the front and back converted photons

$$F(\gamma_p) = \frac{1}{2}\left(\frac{n_p^{\rm front}}{E_p^{\rm front}} + \frac{n_p^{\rm back}}{E_p^{\rm back}}\right)\frac{1}{\delta\Omega_{N_{\rm pix}}}\,. \tag{10}$$

For the pixels outside of the window we put $F(\gamma_p) = 0$. The spherical harmonics decomposition of the flux is

$$F_k = \sum_{p=1}^{N_{\rm pix}} Y_k^*(\gamma_p) F(\gamma_p)\frac{4\pi}{N_{\rm pix}} \tag{11}$$

$$= \sum_{p=1}^{N_{\rm pix}} Y_k^*(\gamma_p)\frac{n_p}{E_p}\,. \tag{12}$$

If we neglect the contribution from point sources, then the variance matrix for F_k is derived similarly to the derivation of the variance in Equation (6)

$$V_{kk'}^{\rm F0} = \sum_{p=1}^{N_{\rm pix}} Y_{k'}^*(\gamma_p) Y_k(\gamma_p)\frac{n_p}{E_p^2} \tag{13}$$

$$= \sum_{p=1}^{N_{\rm pix}} Y_{k'}^*(\gamma_p) Y_k(\gamma_p)\frac{F(\gamma_p)}{E(\gamma_p)}\frac{4\pi}{N_{\rm pix}}\,. \tag{14}$$

This is simply the k' Fourier harmonic of $Y_k(\gamma)\frac{F(\gamma)}{E(\gamma)}$.[2] In Appendix B we show that at angular scales smaller than the PSF, the point sources increase the variance. If $m_{\rm av}$ is the average number

[2] In actual calculations we use the spherical functions with normalization $\tilde{Y}_{lm} = \sqrt{4\pi}Y_{lm}$. In this case $F_k = \frac{N_{\rm pix}}{\sqrt{4\pi}}\sum_{p=1}^{N_{\rm pix}} Y_k^*(\gamma_p)\frac{n_p}{E_p}\frac{4\pi}{N_{\rm pix}}$ and $V_{kk'}^{\rm F0} = N_{\rm pix}\sum_{p=1}^{N_{\rm pix}} Y_{k'}^*(\gamma_p)Y_k(\gamma_p)\frac{n_p}{E_p^2}\frac{4\pi}{N_{\rm pix}}$.

of photons from the point sources, then the actual variance matrix is

$$V^{\rm F}_{kk'} = m_{\rm av} V^{\rm F0}_{kk'}. \tag{15}$$

We will use this expression for the variance matrix in the calculations below. The values of $m_{\rm av}$ for energy bins above 3 GeV are found in Appendix B.

Let us stress that F_k and $V^{\rm F}_{kk'}$ are the best estimates that we can make about the true values of the average harmonic decomposition coefficients and their variance among different realizations based on a single map of photons that we have.[3] The gamma-ray data in our approach are represented by F_k and $V^{\rm F}_{kk'}$. The other quantities considered in the paper, such as the best fit fluxes for various templates and the variance of these fluxes, depend on the data through F_k and $V^{\rm F}_{kk'}$ and on the models through the spherical decomposition of the templates.

Denote by $f^\alpha(\gamma)$ the PDFs of some model fluxes, $\alpha = 1, \ldots, N_{\rm models}$. The corresponding harmonic decomposition coefficients are

$$V^\alpha_k = \sum_{p=1}^{N_{\rm pix}} Y^*_k(\gamma_p) f^\alpha(\gamma_p) \frac{4\pi}{N_{\rm pix}}\,. \tag{16}$$

In Fourier space, the problem of fitting the observed flux by the model fluxes F_α is reduced to minimizing the length of the vector

$$v_k = F_k - \sum_{\alpha=1}^{N_{\rm models}} F_\alpha V^\alpha_k\,, \tag{17}$$

in a space with the metric given by the covariance matrix $C^{\rm F}_{k'k}$ which is the inverse of the variance matrix in Equation (15).

As before, F_k are the harmonic decomposition coefficients of the data, F_α are the total fluxes inside the window corresponding to the templates $\alpha = 1, \ldots, N_{\rm models}$, and V^α_k are the harmonic decomposition coefficients of the templates PDFs. Note, that Equation (17) is linear in the model parameters F_α. Consequently, the minimization obtained by varying F_α is a linear operation. The χ^2 is defined as the norm of the vector v_k squared

$$\chi^2 \equiv \sum_{k'k} C^{\rm F}_{k'k} v^*_{k'} v_k \tag{18}$$

[3] A useful analogy here is the Poisson distribution. Suppose that we can make a single Poisson draw and the result is a number N, then the best estimates for the average and the variance will be N and N^2 respectively. The true values may be different, but we cannot find them based on a single draw.

where the star denotes complex conjugate. The number of components of the vector v_k is determined by the number of Fourier harmonics which are above the Poisson noise. In practice, we will usually use the Y_{l0} harmonics for most of the calculations with l ranging from 0 to 10 or 15. For the current number of observed gamma-ray events, higher l harmonics are dominated by the noise for most of the energy bins (cf., the intermediate energy bins in Figure 6, Appendix B).

The minimal χ^2 is obtained for

$$F_\alpha = \sum_\beta {M^{-1}}_{\alpha\beta} X^\beta \,, \tag{19}$$

where M^{-1} is the inverse of $M^{\alpha\beta} = (\mathbf{V}^\alpha \cdot \mathbf{V}^\beta)$ and $X^\beta = (\mathbf{F} \cdot \mathbf{V}^\beta)$. Here $\mathbf{F} = \{F_k\}$ is the vector of the data Fourier transform coefficients, $\mathbf{V}^\alpha = \{V_k^\alpha\}$ is the vector of the template α Fourier transform coefficients and the dot denotes the scalar product with metric $C^{\rm F}_{k'k}$, for instance,

$$(\mathbf{V}^\alpha \cdot \mathbf{V}^\beta) = \sum_{k'k} C^{\rm F}_{k'k} V^{\alpha *}_{k'} V^\beta_k \,. \tag{20}$$

The variance matrix is

$$\langle \delta F_\alpha \delta F_\beta \rangle = \sum_{\gamma\rho} {M^{-1}}_{\alpha\gamma} \langle \delta X^\gamma \delta X^\rho \rangle {M^{-1}}_{\rho\beta} \,. \tag{21}$$

Since the vectors $\mathbf{V}^\alpha$ are constant, $\delta X^\alpha = (\delta\mathbf{F} \cdot \mathbf{V}^\alpha)$. The variation of the data vector $\delta\mathbf{F}$ is given by the variance matrix $V^{\rm F}$. It is easy to show that $\langle \delta X^\gamma \delta X^\rho \rangle = (\mathbf{V}^\gamma \cdot \mathbf{V}^\rho) = M^{\gamma\rho}$. Thus the variance matrix for the model fluxes F_α is (cf., Press et al. 2007)

$$\langle \delta F_\alpha \delta F_\beta \rangle = {M^{-1}}_{\alpha\beta} \,. \tag{22}$$

In particular, the variance of F_α is

$$\mathrm{Var}(F_\alpha) = {M^{-1}}_{\alpha\alpha} \,. \tag{23}$$

We will use this expression as an estimation of the uncertainties in the model fluxes. These uncertainties depend both on the variance of the data through the covariance matrix $V^{\rm F}$ and on the choice of the model through the Fourier decomposition V_k^α of the template PDFs. Any model, that is used to find the DM fraction in a finite amount of data, introduces an uncertainty due to errors in the identification of the DM fraction. This uncertainty is additional to the data Poisson noise. In the next subsection we will show that the uncertainties in Equation (23) provide an adequate estimation of the data Poisson noise together with the model uncertainties due to DM fraction miscalculation.

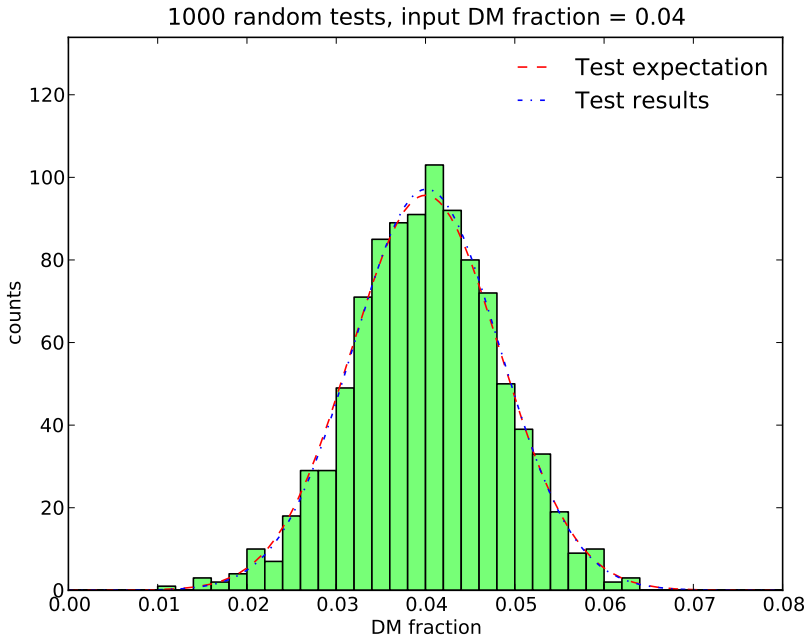

Fig. 1.— Test of the Fourier transform algorithm for separating the DM contribution from an isotropic background. Test expectation of the DM fraction is $(4.00 \pm 0.83) \times 10^{-2}$. The DM fraction in 1000 tests is $(4.01 \pm 0.82) \times 10^{-2}$. The relative deviation of the mean is $1/\sqrt{1000} \approx 0.03$. Both the DM fraction and the standard deviation are within 1-sigma deviation of the mean from the theoretical expectations. The number of degrees of freedom is 14 (there are 16 Y_{l0} harmonics and 2 fitting coefficients). The measured χ^2 is 14.5 ± 5.4.

2.3. Monte Carlo test

In this subsection we check our method for separating the DM fraction by generating random distributions of photons. For the test we use an isotropic distribution of photons plus a distribution of photons coming from DM annihilation in an NFW profile (Navarro et al. 1997)

$$\rho_{\rm DM}(r) \propto \frac{r}{r_s} \frac{1}{(1 + r/r_s)^2} \tag{24}$$

with the scale parameter $r_s = 20$ kpc (e.g., Smith et al. 2007; Xue et al. 2008).

We use the following fixed model parameters (they will be later used for the actual data):

1. Window: $\theta \in (20^\circ,\ 160^\circ)$, $\varphi \in (-70^\circ,\ 70^\circ)$ plus the symmetric part in the Northern hemisphere $\varphi \in (180^\circ - 70^\circ,\ 180^\circ + 70^\circ)$

2. Y_{lm} harmonics: $l = 0, \ldots, 15$ and $m = 0$.

3. HEALPix parameter nSide = 16. The total number of pixels is $12 \times \text{nSide}^2$.

The average total number of photons inside the window is 10^4 with an average fraction of photons coming from DM annihilation 0.04. In every pixel p we put a random number of photons n_p according to the Poisson distribution with an average equal to the combined density at that pixel $\mu_p = \mu_p^{\rm isotr} + \mu_p^{\rm DM}$. Thus the number of DM photons generated for every realization of the map has a Poisson distribution with the average 400 and the standard deviation $20 = \sqrt{400}$. Consequently, the Poisson noise due to random generation of the maps gives the minimal uncertainty in the determination of the DM fraction in this test, $q^{\rm DM} = 0.04 \pm 0.002$. Any method of determining the DM fraction will increase this uncertainty due to errors in separating the DM photons from other distributions (the isotropic distribution in our case).

In the test we generated $N_{\rm tests} = 1000$ realizations of the photon map. For every realization i, we find a best estimate of the DM fraction $q_i^{\rm DM}$. The average among the realization and the standard deviation are denoted by $\mu_{\rm test}$ and $\sigma_{\rm test}$. The obtained values are $\mu_{\rm test} = 4.01 \times 10^{-2}$ and $\sigma_{\rm test} = 0.82 \times 10^{-2}$.

An alternative way to calculate the standard deviation of the DM fraction is to find $\sigma_i^{\rm DM}$ for every realization of the photon map as the square root of the variance in Equation (23). The average of the best estimate standard deviations over the realizations of the map is the "expected" standard deviation $\sigma = 0.83 \times 10^{-2}$.

The expected deviation of the mean is $\sigma/\sqrt{N_{\rm tests}} \approx 0.03 \times 10^{-2}$. Thus the actual deviation of the mean DM fraction from the expected value is less than one sigma. Also the difference of the actual standard deviation and the expected one is less than one sigma. We conclude that, given a particular distribution of photons, the best estimate variance in Equation (23) is an adequate representation of the actual variance among the realizations of the photon distribution. The results of the test are shown in Figure 1.

The $\chi^2 = 14.5 \pm 5.4$ is calculated from Equation (18). The number of degrees of freedom is fourteen: there are sixteen data points corresponding to Y_{l0} harmonics for $l = 0, \ldots, 15$ and two varying parameters corresponding to the normalization of the two templates: isotropic and DM.

3. Bin to bin fitting

In this section we apply the method described in the previous section to 13 months of *Fermi* gamma-ray data that belong to the "diffuse class" (Class 3) of the LAT pipeline. When

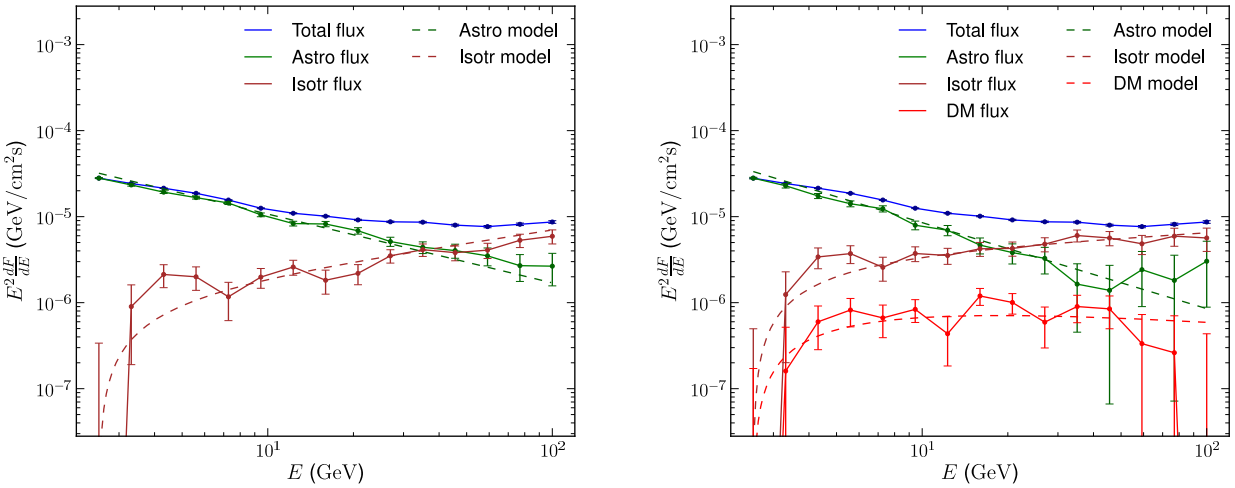

Fig. 2.— Left plot: results of a two-model fitting (astrophysics template and isotropic distribution). The points represent the fitting in every energy bin independently (Table 1). Dashed lines: global fitting by power-law fluxes, the indices of the power laws are given in the first row of Table 3. In global fitting we skip the first two bins (the first bin is "singular" since we use it for the astro template and the second bin is correlated with the first one). Right plot: a gamma-ray source with the morphology of DM annihilation in an NFW profile is added (Table 2). The parameters of the best fit power-law fluxes are given in the "annihilation" line of Table 1. The fitting procedure and the parameters are described in the Monte-Carlo test in Section 2.

the satellite passes through the South Atlantic Anomaly (SAA) the cosmic rays contamination increases. Therefore, we exclude the gamma-ray data taken at those times. Also we exclude the data taken beyond zenith angles of 105° due to significant contamination from atmospheric gamma-rays.

We separate the gamma-rays in exponential energy bins. The binning is the same as the binning used by the *Fermi* collaboration in the diffuse gamma-ray model.[4] The centers of the bins are described by $E_n = E_0 e^{n\Delta}$ MeV where $E_0 = 50$ MeV and $\Delta = \frac{1}{29}\log\frac{10^5\text{MeV}}{50\text{MeV}}$ so that $E_{29} = 100$ GeV. We will mostly consider energies above 1 GeV.

At first we fit the data by a combination of two templates: the astrophysical template that we model by the low energy bin centered around $E = 2.55$ GeV and the isotropic flux. The choice of the "astro" template energy is motivated by the following reasons:

[4] `http://fermi.gsfc.nasa.gov/ssc/data/access/lat/BackgroundModels.html` .

1. If we take a higher energy "astro" template, then we get more conservative bounds on DM signal (since larger fraction of DM signal is considered to be a part of the "astro" background). But if the astro template energy is too high, we will have no non-trivial bins that are not dominated by the Poisson noise. By taking 2.55 GeV astro template, we obtain both conservative and non-trivial DM signal.

2. In the next section we fit the templates in all bins assuming a simple power-law dependence on the energy. This single power-law dependence is not adequate for astro templates with $E \lesssim 2.55$ GeV. Although this condition is not fundamental, it simplifies the fitting procedure significantly.

3. For the calculation of the variance matrix we need to know the contribution from the point sources. We were able to disentangle this contribution for energies above 2.55 GeV (see Appendix B).

The fixed model parameters are the same as in the random test in the previous section. The ratio of the best fit template fluxes to the total flux in every energy bin is shown in Table 1. We also compare the fluxes on the left plot of Figure 2.

In the second case we add a template corresponding to DM annihilating in an NFW profile (Equation (24)) normalized to the local DM density $\rho_{\rm DM0} = 0.4\,{\rm GeVcm}^{-3}$ (e.g., Catena & Ullio 2009; Weber & de Boer 2010; Salucci et al. 2010). As before, we take $r_s = 20$ kpc. The window angle $\theta > 20^\circ$ corresponds to distances $r > 3$ kpc from GC. At these distances the NFW profile is similar to less cuspy profiles, such as the Einasto profile (Navarro et al. 2004). We assume $R_0 = 8.5$ kpc throughout the analysis (e.g., Gillessen et al. 2009; Bovy et al. 2009).

The best fit fluxes for the low energy bin template, for the isotropic template, and for the DM template are shown in Table 2 and on the right plot of Figure 2. We notice that in some energy bins the significance of DM fraction is above three sigma. We also present an example of the a_{lm}'s in the $E = 15.97$ GeV energy bin in Figure 3.

A specific feature of our "astrophysics" template is that it takes all photons in $E = 2.55$ GeV energy bin. Although we expect that the flux at this energy is dominated by the astrophysical sources in our Galaxy, there may be a significant contribution from the extra-galactic sources and from DM. Thus the fits for the isotropic and DM fluxes represent the difference between the fluxes in higher energy bins and the flux in $E = 2.55$ GeV bin. In the next section we fit global models in all energy bins in a way that takes this peculiarity into account. In this section we use the information on the difference of DM fluxes in order to put limits on DM annihilation into

E (GeV)	$N_{photons}$	F_{total} ($GeV^{-1}cm^{-2}s^{-1}$)	astro frac	isotr frac	χ^2
2.55	96236	4.3×10^{-6}	1.00 ± 0.01	0.00 ± 0.01	0.0
3.31	64003	2.2×10^{-6}	0.96 ± 0.03	0.04 ± 0.03	7.8
4.31	43491	1.2×10^{-6}	0.90 ± 0.03	0.10 ± 0.03	12.9
5.60	29488	6.0×10^{-7}	0.89 ± 0.03	0.11 ± 0.03	22.4
7.27	19647	2.9×10^{-7}	0.92 ± 0.04	0.08 ± 0.04	15.0
9.45	12334	1.4×10^{-7}	0.84 ± 0.04	0.16 ± 0.04	23.4
12.28	8500	7.3×10^{-8}	0.76 ± 0.05	0.24 ± 0.05	20.7
15.97	6080	4.0×10^{-8}	0.81 ± 0.06	0.18 ± 0.06	32.8
20.75	4288	2.1×10^{-8}	0.75 ± 0.06	0.24 ± 0.06	39.3
26.97	3216	1.2×10^{-8}	0.59 ± 0.07	0.40 ± 0.07	19.8
35.05	2471	7.0×10^{-9}	0.51 ± 0.08	0.48 ± 0.08	20.6
45.55	1745	3.8×10^{-9}	0.51 ± 0.09	0.48 ± 0.09	21.8
59.20	1265	2.2×10^{-9}	0.46 ± 0.11	0.53 ± 0.11	11.8
76.94	1014	1.4×10^{-9}	0.33 ± 0.11	0.65 ± 0.12	16.2
100.00	811	8.7×10^{-10}	0.31 ± 0.13	0.68 ± 0.13	9.2

Table 1: The results of fitting the data with the "astrophysics" template and the isotropic distribution of gamma-rays. For the astrophysics template we choose the $E = 2.55$ GeV energy bin (the model in the first row fits the data exactly by definition). The "astro frac" and the "isotr frac" columns represent the fractions of gamma-rays distributed according to the "astro" template and to the isotropic distribution. The corresponding fluxes are obtained by multiplying with the total flux (we allow that the "astro" and the isotropic fluxes do not necessarily add up to the total flux due to the Poisson fluctuations of $F_{\rm total}$). We represent the data by Y_{l0} harmonics with $l = 0, \ldots, 15$. Consequently, there are 16 - 2 = 14 degrees of freedom in every bin.

monochromatic photons.

Let $\langle \sigma v \rangle_{\rm line}$ denote the cross section for DM particles to annihilate into a pair of photons. These photons are monochromatic with energies $E = M_{\rm DM}$. The corresponding flux per steradian at angle θ from the GC is

$$F_{\rm DM\,line}(E, \theta) = 2 \frac{1}{8\pi} \frac{\langle \sigma v \rangle_{\rm line}}{M_{\rm DM}^2} \int \rho_{\rm DM}^2(r) dR \tag{25}$$

where R is the distance from the Earth and r is the distance from GC, i.e., in terms of the vectors $\mathbf{r} = \mathbf{R} + \mathbf{R}_0$ and $r^2 = R^2 + R_0^2 + 2RR_0 \cos\theta$. The factor of 2 is due to the fact that there are two photons created in each annihilation event. Since $E = M_{\rm DM}$, then $E^2 F_{\rm DM\,line}(E, \theta)$ does not

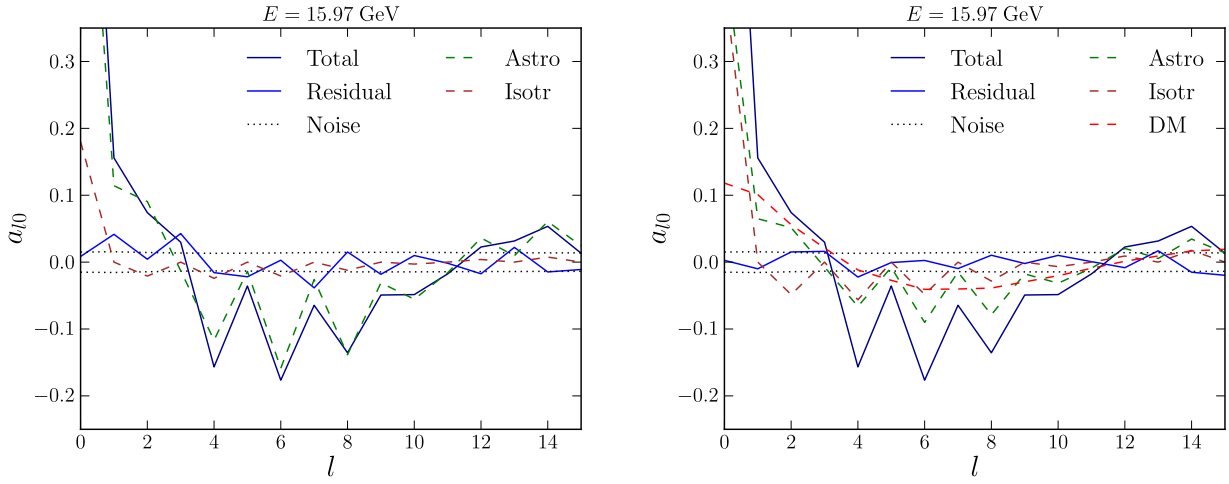

Fig. 3.— An example of the a_{lm} fitting procedure for $m = 0$ and $l = 0, \ldots, 15$ in the $E = 15.97$ GeV energy bin. We use the harmonic decomposition in a window defined in Section 2.3. The a_{lm}'s are normalized to the total flux in this energy bin. The "Astro" a_{lm}'s are given by the gamma-ray map decomposition in the $E = 2.55$ energy bin. The "Isotropic" a_{lm}'s are non-zero for $l > 0$ due to the spherical harmonics decomposition in a window, otherwise only a_{00} component would have been non-trivial. The "DM" component corresponds to NFW annihilation (it is described in Section 3). The "Residual" a_{lm}'s are defined as the total flux a_{lm}'s minus the templates' a_{lm}'s. The "Noise" level corresponds to the square root of the diagonal elements in the variance matrix in Equation (15). This variance matrix is not diagonal and the χ^2 recieves contributions from non-diagonal elements as well. The χ^2 for the two-template fit (left plot) is 32.8 for 14 dof (Table 1). The χ^2 for the three-template fit (right plot) is 12.7 for 13 dof (Table 2).

depend on the energy. The expected DM line flux integrated over our window is

$$E^2 \int F_{\rm DM\,line}(E,\theta) d\Omega = \frac{\langle \sigma v \rangle_{\rm line}}{\langle \sigma v \rangle_0}\, 1.5 \times 10^{-4} \frac{\rm GeV^2}{\rm cm^2 s} \tag{26}$$

where $\langle \sigma v \rangle_0 = 3 \times 10^{-26} {\rm cm^3 s^{-1}}$ is the standard freeze out annihilation cross section. The DM line flux can be compared to the upper limits on the DM fraction in Table 2. For instance, a two sigma limit is obtained as $(q^i_{\rm DM} + 2\sigma^i_{\rm DM}) E_i^2 F_{\rm total}(E_i) \Delta E_i$, where E_i and ΔE_i are the center and the width of the i'th bin. The limits on $\langle \sigma v \rangle_{\rm line}$ in units of the standard freeze out cross section are shown in the last column of Table 2. These simple estimates are a factor of a few less constraining than the limits on monochromatic gamma-rays obtained by *Fermi* collaboration (Abdo et al. 2010).

According to our fits, the best fit energy spectrum for the DM component is rather smooth.

E (GeV)	$N_{photons}$	F_{total} ($GeV^{-1}cm^{-2}s^{-1}$)	astro frac	isotr frac	DM frac	χ^2	$\langle\sigma v\rangle_{line}$ $3\times10^{-26}cm^3s^{-1}$
2.55	96236	4.3×10^{-6}	1.00 ± 0.02	0.00 ± 0.02	0.00 ± 0.01	0.0	0.0
3.31	64003	2.2×10^{-6}	0.94 ± 0.06	0.05 ± 0.04	0.01 ± 0.01	7.6	<0.005
4.31	43491	1.2×10^{-6}	0.81 ± 0.06	0.16 ± 0.04	0.03 ± 0.01	9.3	<0.009
5.60	29488	6.0×10^{-7}	0.76 ± 0.06	0.20 ± 0.05	0.04 ± 0.02	14.8	<0.013
7.27	19647	2.9×10^{-7}	0.79 ± 0.07	0.17 ± 0.05	0.04 ± 0.02	9.0	<0.015
9.45	12334	1.4×10^{-7}	0.63 ± 0.07	0.30 ± 0.06	0.07 ± 0.02	11.9	<0.021
12.28	8500	7.3×10^{-8}	0.63 ± 0.09	0.32 ± 0.07	0.04 ± 0.02	17.6	<0.019
15.97	6080	4.0×10^{-8}	0.46 ± 0.10	0.42 ± 0.08	0.12 ± 0.03	12.7	<0.047
20.75	4288	2.1×10^{-8}	0.42 ± 0.11	0.47 ± 0.09	0.11 ± 0.03	25.3	<0.054
26.97	3216	1.2×10^{-8}	0.38 ± 0.13	0.55 ± 0.10	0.07 ± 0.03	15.7	<0.054
35.05	2471	7.0×10^{-9}	0.19 ± 0.14	0.70 ± 0.11	0.10 ± 0.04	12.4	<0.091
45.55	1745	3.8×10^{-9}	0.17 ± 0.17	0.71 ± 0.13	0.11 ± 0.04	16.0	<0.119
59.20	1265	2.2×10^{-9}	0.32 ± 0.20	0.63 ± 0.16	0.04 ± 0.05	11.0	<0.112
76.94	1014	1.4×10^{-9}	0.22 ± 0.21	0.73 ± 0.17	0.03 ± 0.05	15.8	<0.149
100.00	811	8.7×10^{-10}	0.35 ± 0.25	0.65 ± 0.20	-0.01 ± 0.06	9.1	<0.184

Table 2: The same as in Table 1 with an extra template corresponding to DM annihilation in an NFW profile. The number of degrees of freedom is 13 in every energy bin. The χ^2 in the intermediate bins between $E = 5.60$ GeV and $E = 45.55$ GeV is significantly reduced compared to the two-model case. The last three energy bins are compatible with the Poisson noise in both cases. The last column represents two-sigma limits on DM annihilation into two photons. The derivation of these limits is presented after Equation (25).

Such a contribution is very hard to detect based only on the energy spectrum of the total flux. The power of the Fourier decomposition lies in its sensitivity to a small fraction of gamma-rays with large scale distribution and possibly smooth energy spectrum. We study the best fit energy spectra for the isotropic background, for the astrophysics, and for the DM in the next section.

In Figure 4 we compare our method with the calculation of Dobler et al. (2010). There is a general agreement above ~ 2 GeV, although our error bars are much larger than the errors of Dobler et al. (2010).

4. Global model

In this section we fit the gamma-ray data by assuming a power-law behavior of the astrophysical and DM fluxes. In the case of DM we also introduce an exponential cutoff. Denote the

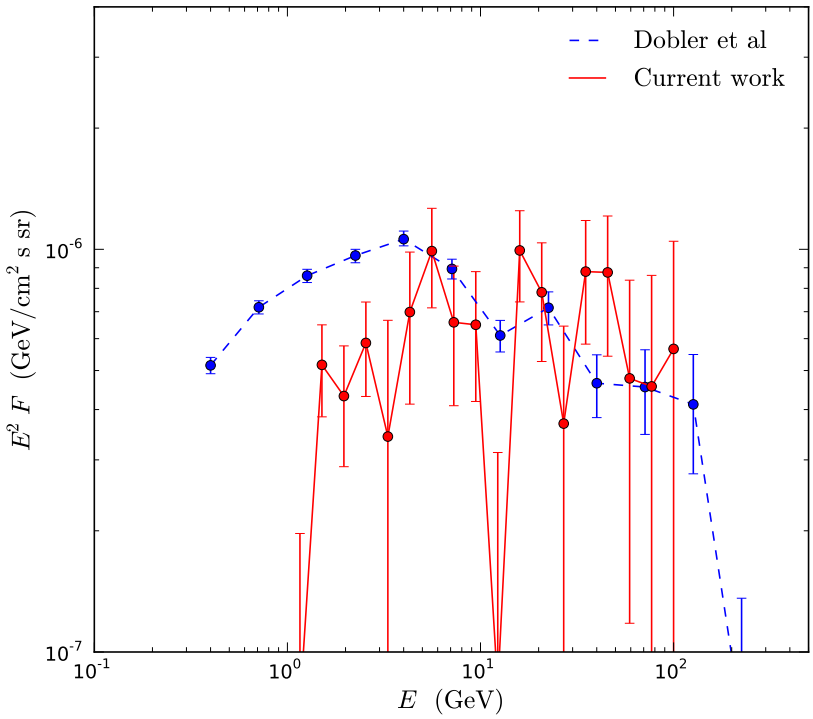

Fig. 4.— Comparison with the gamma-ray haze found by Dobler et al. (2010). In the derivation we use a three-template fitting: astrophysics model given by gamma-rays in $E = 0.1$ GeV energy bin, isotropic distribution, and an additional source with the gaussian bivariate morphology $\sigma_l = 15^\circ$, $\sigma_b = 25^\circ$ (Dobler et al. 2010). The fluxes correspond to the gaussian bivariate template. We fit in the window described in Section 2. The presented values are computed by averaging over $l \in (-15^\circ,\ 15^\circ)$ and $b \in (-30^\circ,\ -10^\circ)$.

non-isotropic (Galactic) component of the flux by $\Phi_{\rm g}(E)$, the extra-galactic isotropic component will be denoted by $\Phi_{\rm i}(E)$, and the DM component by $\Phi_{\rm d}(E)$.

In the previous section we were fitting the data by taking a low energy bin as a template for the Galactic astrophysical component. In reality the flux in the first bin E_0 is a sum of all three components

$$F_{\rm a}(E_0) = \Phi_{\rm g}(E_0) + \Phi_{\rm i}(E_0) + \Phi_{\rm d}(E_0)\,. \tag{27}$$

The corresponding template has contributions from the actual Galactic photons, from the isotropic distribution, and from the DM. Consequently, a fraction of isotropic and DM photons contributes to the "astrophysics" flux at all energies.

Model	$n_{\rm g}$	$n_{\rm i}$	$n_{\rm d}$	$E_{\rm cut}$ (GeV)	χ^2	dof
No DM	2.8	1.5	-	-	337	204
Decay	2.9	1.5	2.0	90	274	201
Annihilation	3.0	1.8	2.2	∞	264	201
Stellar halo	3.0	1.7	1.8	60	260	201
Gaussian halo	3.0	1.8	1.8	90	267	201

Table 3: The results of fitting the data by the power-law "Galactic", "isotropic", and "DM" fluxes. The expression of these fluxes in terms of the fluxes corresponding to the low energy bin template, the isotropic template and the DM template is explained in the text. "Decay" and "Annihilation" denote DM decay and annihilation in an NFW profie. "Stellar halo" denotes a source following the mass distribution in the stellar halo of the Milky Way $\propto 1/r^3$ (e.g., Jurić et al. 2008). "Gaussian halo" denotes the bivariate gaussian profile with $\sigma_l = 15^\circ$ and $\sigma_b = 25^\circ$ used by Dobler et al. (2010). In the case of annihilation, decay and stellar halo, the cutoff tends to infinity, i.e., the corresponding fluxes are simple power-laws. In fitting we use Y_{lm}'s with $l = 0, \ldots, 15$ for 13 energy bins above 4 GeV (the first two energy bins are excluded). Thus, we have $13 \times 16 = 208$ numbers to fit with 4 parameters in the two-template model (the first row) and with 7 parameters in the three-template models.

We will take the following parameterization of the "real" fluxes

$$\Phi_{\rm g} = \Phi_{\rm g0}(E/E_0)^{-n_{\rm g}}\,, \tag{28}$$

$$\Phi_{\rm i} = \Phi_{\rm i0}(E/E_0)^{-n_{\rm i}}\,, \tag{29}$$

$$\Phi_{\rm d} = \Phi_{\rm d0}(E/E_0)^{-n_{\rm d}} e^{-(E-E_0)/E_{\rm cut}}\,. \tag{30}$$

If we assume that the Galactic gamma-rays provide the most significant contribution to the astro template at E_0, then we can expect that the astro template flux $F_{\rm a}$ has the same power-law index as the "real" Galactic flux $\Phi_{\rm g}$ and the following parameterization of $F_{\rm a}$ is reasonable:

$$F_{\rm a}(E) = (\Phi_{\rm g0} + \Phi_{\rm i0} + \Phi_{\rm d0})\,(E/E_0)^{-n_{\rm g}}\,. \tag{31}$$

The fluxes for the isotropic and DM templates are equal to the real fluxes minus the contribution to the "astro" template:

$$F_{\rm i}(E) = \Phi_{\rm i0}(E/E_0)^{-n_{\rm i}} - \Phi_{\rm i0}(E/E_0)^{-n_{\rm g}}\,, \tag{32}$$

$$F_{\rm d}(E) = \Phi_{\rm d0}(E/E_0)^{-n_{\rm d}} e^{-(E-E_0)/E_{\rm cut}} - \Phi_{\rm d0}(E/E_0)^{-n_{\rm g}}\,. \tag{33}$$

In Table 3 we present the results of fitting of the fluxes $F_{\rm a}$, $F_{\rm i}$, and $F_{\rm d}$ to the data. We compare five cases. In the first case we take only two fluxes $F_{\rm a}$ and $F_{\rm i}$. The other four cases

have an additional flux $F_{\rm d}$ with a spherical morphology. For the case of decaying DM and annihilating DM we use the NFW profile. After that we consider a source of gamma-rays in the stellar halo of the Milky Way, such as the millisecond pulsars (Malyshev et al. 2010) (see also Faucher-Giguère & Loeb (2010) for the millisecond pulsars contribution to gamma-rays in the Galactic disk). We assume that the profile of this source follows the distribution of the mass in the stellar halo $\propto 1/r^3$ (Bell et al. 2008; Jurić et al. 2008). In the last case we assume a Gaussian bivariate profile with $\sigma_l = 15^\circ$ and $\sigma_b = 25^\circ$ as used by Dobler et al. 2010. We have used the energy bins between $E_{\rm min} = 4.3$ GeV and $E_{\rm max} = 100$ GeV for fitting. The best fit is obtained for the stellar halo, followed by DM annihilation, Gaussian distribution, and DM decay. These results are very sensitive to the energy range used for fitting and are not conclusive. The best fit has $\chi^2/{\rm dof} \approx 1.3$ for the stellar halo.

5. Conclusions

In this paper we argue that the Fourier transform is a sensitive tool to study the large scale distribution of gamma-rays such as a possible contribution from DM annihilation or decay. The key points of this approach are the use of the Fourier decomposition in a window that eliminates most of the known astrophysical sources and the choice of the coordinate system appropriate for the symmetries of DM distribution. We show that in a test with 10^4 randomly generated photons, a 4% fraction of gamma-rays coming from DM annihilation can be detected with a four sigma significance.

One of the main advantages of the Fourier transform compared to the analysis in coordinate space is an efficient organization of the data. Let us take, as an example, the top left plot in Figure 6. One can clearly see that harmonics with $l \lesssim 100$ carry some information while harmonics above 100 are dominated by the noise (either physical noise due to insufficient statistics or the PSF of the instrument). Thus we immediately know the maximal amount of information and its precision. The comparison with the Fourier transform of templates is straightforward (the main problem is to find good, physically motivated templates). It is also clear how to evaluate consistency of current data with the future data either from the same instrument or from another experiment that may have a completely different PSF: the vectors representing the Fourier harmonics should be within the Poisson noise.

Another approach in finding DM signatures in gamma-rays actively discussed in the literature is to search for features in the power spectrum due to DM subhalos (Ando 2009; Hensley et al.

2009; Cuoco et al. 2010). Our method is complimentary to this, since we look for the signature of the main halo at small l, whereas DM subhalos usually contribute at $l \gtrsim 100$. We also believe that with the current amount of data our approach is more advantageous since $l \gtrsim 100$ harmonics are still dominated by the noise and much more data will be necessary to separate a significant signal, whereas for small l the current data is enough to overcome the noise level for energies up to $30 - 50$ GeV.

Our method already enables us to argue that there is a significant spherical distribution of photons in addition to an astrophysical template modeled by a low energy bin plus an isotropic distribution of photons. Also, assuming a power law dependence of fluxes on energy, we find that the DM annihilation or a stellar halo source are slightly more preferable than either DM decay or a bivariate gaussian distribution found by Dobler et al. (2010). These conclusions are preliminary, since the method is very sensitive to the energy range used to fit the energy spectrum and on the functional dependence on energy. We expect to get better limits on DM fraction, shape of the profile, and the energy spectrum with two years of *Fermi* data.

A. Variations of the main model

In this appendix we study the dependence of the gamma-ray fraction coming from a spherical source on model parameters. As a reference model we take DM annihilation with the following parameters:

- $\theta_0 = 20^\circ$, $\varphi_0 = 70^\circ$. The window is: $\theta \in (\theta_0,\ 180^\circ - \theta_0)$, $\varphi \in (-\varphi_0,\ \varphi_0)$ plus the symmetric part in the Northern hemisphere $\varphi \in (180^\circ - \varphi_0,\ 180^\circ + \varphi_0)$
- Y_{lm} harmonics: $L_{\min} = 0$, $L_{\max} = 15$, $m = 0$
- HEALPix parameter nSide = 16
- Astrophysics template energy bin, $E_{\min} = 2.55$ GeV

The main model is represented by circles with error bars in Figure 5. Dashed lines in this figure represent the following variations of the main model:

1. Shrinking the window size to $\theta_0 = 30^\circ$ makes the fraction smaller around 40 GeV. This may be a statistical fluctuation, or it may be due to a cuspy profile of gamma-rays at high energies.

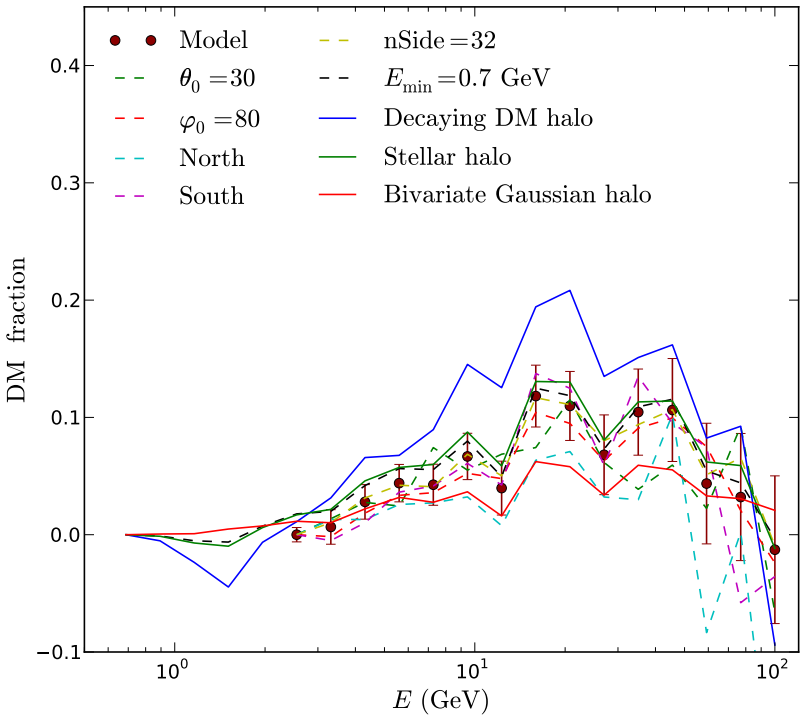

Fig. 5.— Dashed lines illustrate dependence of DM fraction on the window and model parameters. Solid lines represent DM-like contributions for different halo profiles. The main model and the variations are described in the text.

2. Increasing the window size to $\varphi_0 = 80^\circ$ doesn't change the DM fraction significantly.

3. Separating the North and South windows: The spherical contribution in the Northern window is significantly smaller than in the Southern Galactic cap. This may be due to a contamination from the Loop 1 in the North. However the total number of events in the North is not significantly larger than the number of events in the South. This fact may be an evidence for an astrophysical origin of the extra signal where such an asymmetry is not as unexpected as in the DM interpretation.

4. DM fraction for a finer grid nSide = 32 is within one sigma deviation from nSide = 16.

5. The last variation corresponds to choosing the astro template model bin $E_{\rm min} = 0.7$ GeV. As was discussed earlier in Section 4, the DM fraction in some bin represents the difference between this bin and the astro model bin. At low energy we expect a smaller contribution from DM. As a result, by reducing the astro template bin energy we increase a possible

DM fraction at higher bins. The two models become compatible at energies $E \gtrsim 10$ Gev.

Solid lines correspond to changing the halo profile for the extra source. In order to increase visibility we use the $E = 0.7$ GeV energy bin for the astro template in these cases. The dashed black line starting at 0.7 GeV is the NFW annihilating DM, the higher blue solid line is the NFW decaying DM, the green solid line in the middle corresponds to stellar-like halo profile $\propto 1/r^3$ and the red lower solid line is the bivariate gaussian distribution. Annihilating DM and stellar halo profiles are very similar to each other.

B. Point sources

In the derivation of the variance of Fourier harmonics in Section 2 we assumed the Poisson distribution of gamma-rays in a small window $\delta\Omega$. In reality this assumption is not always true. Due to a presence of point sources, some photons may be correlated with others and the Poisson statistics is violated.

Denote by $\langle \delta n_m \rangle$ the average number of m-photon sources inside a small window $\delta\Omega$. We will assume that the sources of photons have a Poisson distribution. The average number of photons is

$$\langle \delta n \rangle = \sum_m m \langle \delta n_m \rangle \,. \tag{B1}$$

The variance is

$$\begin{aligned} \mathrm{Var}(\delta n) &= \sum_m m^2 (\langle \delta n_m^2 \rangle - \langle \delta n_m \rangle^2) \\ &= \sum_m m^2 \langle \delta n_m \rangle \,. \end{aligned}$$

In the Poisson statistics case $\langle \delta n_m \rangle = 0$ for all $m \neq 1$ and the variance is equal to the total number of photons $\mathrm{Var}(\delta n) = \langle \delta n_1 \rangle = \langle \delta n \rangle$. If $\langle \delta n_m \rangle \neq 0$ for some $m \neq 1$ then

$$\sum_m m^2 \langle \delta n_m \rangle > \sum_m m \langle \delta n_m \rangle = \langle \delta n \rangle \,. \tag{B2}$$

Consequently, the variance in the presence of point sources is larger than the variance in the Poisson statistics case. Denote by m_{av} the average number of photons from the point sources

$$m_{\mathrm{av}} = \frac{\sum_m m^2 \langle \delta n_m \rangle}{\sum_m m \langle \delta n_m \rangle} \,. \tag{B3}$$

With this definition, the variance matrix in the presence of point sources is $m_{\rm av}$ times larger than the variance matrix in the Poisson statistics case. Thus, the variance derived in Equation (13) should be multiplied by $m_{\rm av}$ and the correct expression for the variance matrix at angular scales smaller than the detector PSF is given by equation (15).

Let us show that in some cases, $m_{\rm av}$ can be found from the properties of the angular power spectrum C_l. As before, given a set of gamma-ray events with coordinates $\gamma_i = (\theta_i,\, \varphi_i)$, define the Fourier transform of their distribution

$$R_{lm} = \sum_{i=1}^{N_{\rm photons}} \tilde{Y}_{lm}(\gamma_i)\,, \tag{B4}$$

where we use the spherical harmonics $\tilde{Y}_{lm} = \sqrt{4\pi} Y_{lm}$. With this normalization, the $\tilde{Y}_{lm}$'s satisfy

$$\frac{1}{2l+1} \sum_{m=-l}^{l} |\tilde{Y}_{lm}(\gamma)|^2 = 1 \tag{B5}$$

for any point γ. If we fix l, then for an isotropic random distribution of photons, R_{lm} is a random walk in $(2l+1)$-dimensional space. The average distance travelled is $\sum_m |R_{lm}|^2 = (2l+1) N_{\rm photons}$. Define $a_{lm} = \frac{1}{N_{\rm photons}} R_{lm}$ and

$$C_l = \frac{1}{2l+1} \sum_m |a_{lm}|^2\,. \tag{B6}$$

If the average $\langle a_{lm} \rangle = 0$, then the variance of a_{lm} is equal to the average of C_l. For a Poisson distribution of photons ${\rm Var}(a_{lm}) = \frac{1}{N_{\rm photons}}$. Consequently, we expect

$$\langle C_l \rangle = \frac{1}{N_{\rm photons}}\,. \tag{B7}$$

for either isotropic distribution of photons or for the angular scales smaller than the detector PSF. We expect this behavior for sufficiently large l.

In the presence of point sources, the variance is $m_{\rm av}$ times larger than the variance in the Poisson statistics case. Consequently, for isotropic distribution of point sources (or when the angular scale corresponding to l is much smaller than the scale of the distribution), we expect

$$\langle C_l \rangle = \frac{m_{\rm av}}{N_{\rm photons}}\,. \tag{B8}$$

In this case the average value of C_l's is a constant larger than $1/N_{\rm photons}$. We expect this behavior for intermediate values of l (at small l, the C_l's are dominated by the large scale structure).

E (GeV)	3.31	4.31	5.60	7.27	9.45	12.3	16.0	20.8	27.0	35.1	45.6	59.2	76.9	100.0
$m_{\rm av}$	3.93	2.76	2.23	1.77	1.52	1.42	1.37	1.25	1.25	1.16	1.12	1.13	1.12	1.03

Table 4: The values of average number of photons $m_{\rm av}$ from point sources (Equation (B3)). The $m_{\rm av}$ is found from the power spectrum C_l in energy bins with a significant plateau at intermediate l's above the Poisson noise expectation.

In Figure 6 we plot the angular spectra for several energy bins. At low energy there is a lot of statistics, $N_{\rm photons} \sim 10^6$, and PSF $> 1^\circ$. In this case the large scale structure dominates below $l \sim 100$ while the PSF noise dominates above $l \sim 100$. For intermediate energies the statistics is smaller than for low energies and the large scale structure dominates C_l's only for $l \lesssim 20 - 30$, while PSF $\sim 0.1^\circ - 1^\circ$. One can clearly see a transition to $m_{\rm av}/N_{\rm photons}$ at $l \sim 30$ followed by a transition to $1/N_{\rm photons}$ above $l \sim 100$. At $E \gtrsim 10$ GeV, PSF $\sim 0.1^\circ$ and the C_l's are consistently above the usual Poisson noise. The values of $m_{\rm av}$ for energy bins where a plateau above $1/N_{\rm photons}$ is visible are shown in Table 4.

In the analysis we use the HEALPix parameter nSide = 2048 which corresponds to approximately 4×10^7 pixels. The "pixelized" values of C_l's are supposed to be smaller than the values computed by a continuous integration, $C_{l\,{\rm pix}} = w_l^2 C_{l\,{\rm cont}}$, where w_l is the pixel window function. The window function is a decreasing function which is equal to 1 at $l = 0$. For nSide = 2048 and $l = 1000$, $w_l^2 \approx 0.978$, i.e. the values of C_l's in Figure 6 are less than about 2.2% smaller than the real values. For nSide = 16 the window function at $l = 15$ is $w_l = 0.957$. We didn't rescale the spherical harmonics by the window function in the fitting procedure. The only effect of the window function is to put a little more weight on lower l harmonics.

Let us make one more technical comment about the derivation of the plots in Figure 6. In order to relate the variance in the Fourier harmonics to the value of C_l's we need that the average $\langle a_{lm} \rangle = 0$. In the analysis we have used the Fourier transform in a window (the window is the same as in Sections 2 and 3). For the Fourier transform in a window, at least some of the expected a_{lm}'s are non-zero. In order to make them zero without affecting the variance we subtract the spherical harmonics of an isotropic distribution inside the window.

Acknowledgments.

The authors are thankful to Douglas Finkbeiner, Jennifer Siegal-Gaskins, Neal Weiner, and especially to David Hogg for valuable discussions and comments. This work is supported in part by the Russian Foundation of Basic Research under Grant No. RFBR 10-02-01315 (D.M.), by the NSF Grant No. PHY-0758032 (D.M.), by DOE OJI Grant No. DE-FG02-06E R41417 (I.C.), by the Mark Leslie Graduate Assistantship (I.C.), by NASA grant NNX08AJ48G (J.B.), and by the NSF grant AST-0908357 (J.B.). Some of the results in this paper have been derived using the HEALPix (Górski et al. 2005) package.

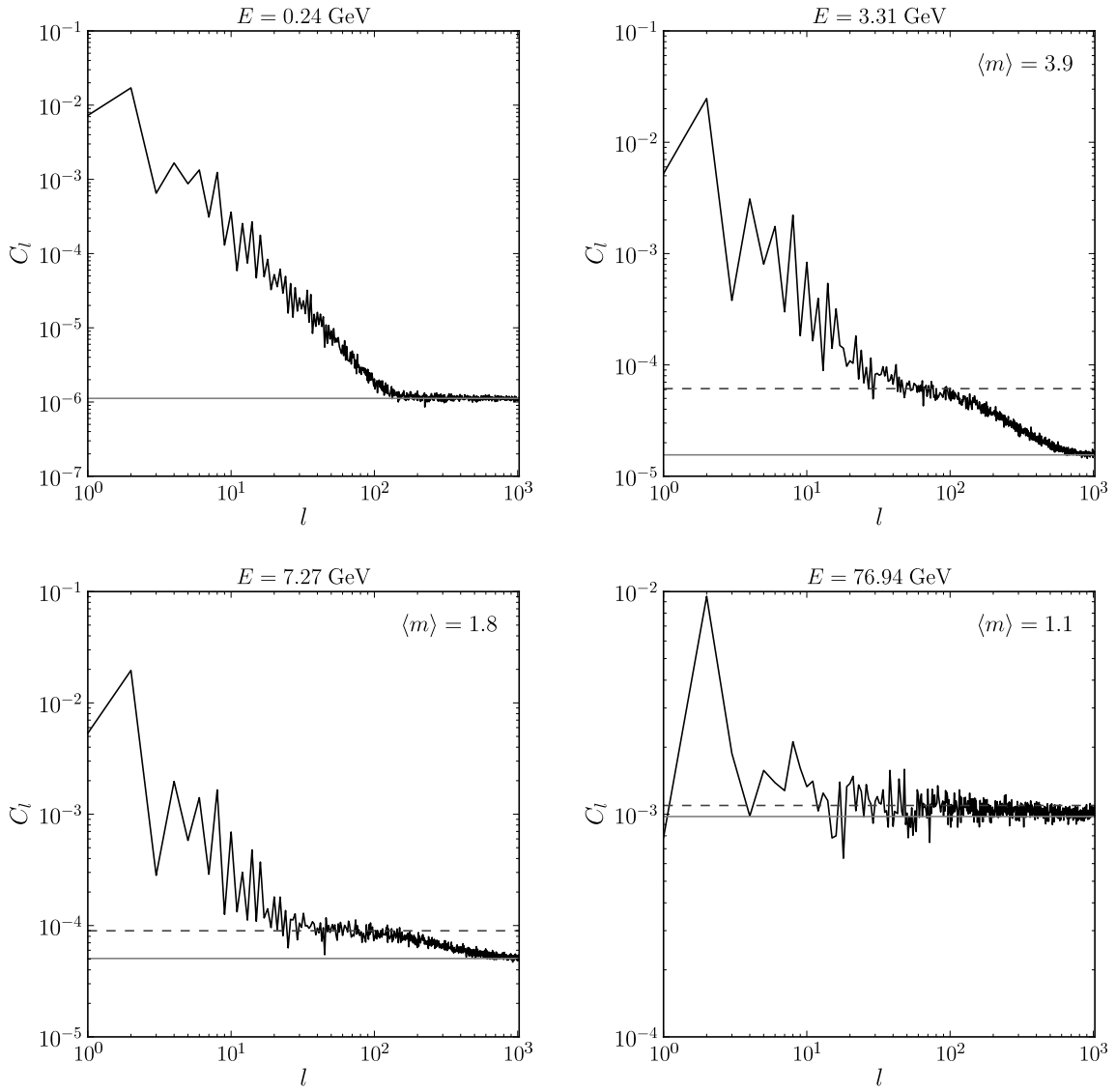

Fig. 6.— Power spectrum of angular modes for gamma-rays inside a window defined in Section 2 and in the beginning of Appendix A. We use the HEALPix parameter nSide = 2048. Solid lines represent the Poisson statistics expectation for either an isotropic distribution of photons or a distribution dominated by the detector PSF. For intermediate energies, there is a clear transition from large scale structure domination to isotropic distribution with a non-trivial contribution of point sources (constant dashed lines above the Poisson level). The ratio of $\langle C_l \rangle$ dominated by the isotropic distribution of point sources to the Poisson distribution average is equal to the average number of photons from the point sources $m_{\rm av} \equiv \langle m \rangle$.

REFERENCES

Abdo, A. A., et al. 2010, PRL, 104, 091302

Ando, S. 2009, Phys. Rev. D, 80, 023520

Bell, E. F., et al. 2008, ApJ, 680, 295

Bovy, J., Hogg, D. W., & Rix, H.-W. 2009, ApJ, 704, 1704

Catena, R., & Ullio, P. 2009, arXiv:0907.0018

Cuoco, A., Sellerholm, A., Conrad, J., & Hannestad, S. 2010, arXiv:1005.0843

Diemand, J., Kuhlen, M., Madau, P., Zemp, M., Moore, B., Potter, D., & Stadel, J. 2008, Nature, 454, 735

Dobler, G., Finkbeiner, D. P., Cholis, I., Slatyer, T., & Weiner, N. 2010, ApJ, 717, 825

Faucher-Giguère, C., & Loeb, A. 2010, Journal of Cosmology and Astro-Particle Physics, 1, 5

Gillessen, S., Eisenhauer, F., Trippe, S., Alexander, T., Genzel, R., Martins, F., & Ott, T. 2009, ApJ, 692, 1075

Górski, K. M., Hivon, E., Banday, A. J., Wandelt, B. D., Hansen, F. K., Reinecke, M., & Bartelmann, M. 2005, ApJ, 622, 759

Hansen, F. K., Górski, K. M., & Hivon, E. 2002, MNRAS, 336, 1304

Hensley, B. S., Siegal-Gaskins, J. M., & Pavlidou, V. 2009, arXiv:0912.1854

Jurić, M., et al. 2008, ApJ, 673, 864

Kuhlen, M., Diemand, J., & Madau, P. 2008, ApJ, 686, 262

Malyshev, D., Cholis, I., & Gelfand, J. D. 2010, arXiv:1002.0587

Navarro, J. F., Frenk, C. S., & White, S. D. M. 1997, ApJ, 490, 493

Navarro, J. F., et al. 2004, Mon. Not. Roy. Astron. Soc., 349, 1039

Press, W. H., Teukolsky, S. A., Vetterling, W. T., & Flannery, B. P. 2007, Numerical Recipes: The Art of Scientific Computing (Cambridge, UK; Cambridge University Press)

Salucci, P., Nesti, F., Gentile, G., & Martins, C. F. 2010, ArXiv:1003.3101

Siegal-Gaskins, J. M., & Pavlidou, V. 2009, PRL, 102, 241301

Smith, M. C., et al. 2007, MNRAS, 379, 755

Springel, V., et al. 2008a, Nature, 456, 73

—. 2008b, MNRAS, 391, 1685

Weber, M., & de Boer, W. 2010, A&A, 509, A25

Xue, X. X., et al. 2008, ApJ, 684, 1143

Zeldovich, Y. B., Klypin, A. A., Khlopov, M. Y., & Chechetkin, V. M. 1980, Sov. J. Nucl. Phys., 31, 664